Langmuir
Article
pubs.acs.org/Langmuir

# Optical Response of Magnetic Fluorescent Microspheres Used for Force Spectroscopy in the Evanescent Field

Alex Bijamov,[†] Fridon Shubitidze,*[,†] Piercen M. Oliver,[‡] and Dmitri V. Vezenov*[,‡]

[†]*Dartmouth College, Thayer School of Engineering, 8000 Cummings Hall, Hanover, New Hampshire 03755, and*
[‡]*Lehigh University, Department of Chemistry, 6 East Packer Avenue, Bethlehem, Pennsylvania 18015*

*Received April 17, 2010*

Force spectroscopy based on magnetic tweezers is a powerful technique for manipulating single biomolecules and studying their interactions. The resolution in magnetic probe displacement, however, needs to be commensurate with molecular sizes. To achieve the desirable sensitivity in tracking displacements of the magnetic probe, some recent approaches have combined magnetic tweezers with total internal reflection fluorescence microscopy. In this situation, a typical force probe is a polymer microsphere containing two types of optically active components: a pure absorber (magnetic nanoparticles for providing the pulling force) and a luminophore (semiconducting nanoparticles or organic dyes for fluorescent imaging). To assess the system's capability fully with regard to tracking the position of the force probe with subnanometer accuracy, we developed a body-of-revolution formulation of the method of auxiliary sources (BOR-MAS) to simulate the absorption, scattering, and fluorescence of microscopic spheres in an evanescent electromagnetic field. The theoretical formulation uses the axial symmetry of the system to reduce the dimensionality of the modeling problem and produces excellent agreement with the reported experimental data on forward scattering intensity. Using the BOR-MAS numerical model, we investigated the probe detection sensitivity for a high numerical aperture objective. The analysis of both backscattering and fluorescence observation modes shows that the total intensity of the bead image decays exponentially with the distance from the surface (or the length of a biomolecule). Our investigations demonstrate that the decay lengths of observable optical power are smaller than the penetration depth of the unperturbed excitation evanescent wave. In addition, our numerical modeling results illustrate that the expected sensitivity for the decay length changes with the angle of incidence, tracking the theoretical penetration depth for a two-media model, and is sensitive to the bead size. The BOR-MAS methodology developed in this work for near-field modeling of bead-tracking experiments fully describes the fundamental photonic response of microscopic BOR probes at the subwavelength level and can be used for future improvements in the design of these probes or in the setup of bead-tracking experiments.

## Introduction

Single-molecule force spectroscopy has developed into a powerful tool for the manipulation of biological molecules and studies of their biophysics.[1] Molecular recognition,[2] protein unfolding,[3] DNA−protein interactions,[4] structural transitions in polysaccharides,[5] the formation of supramolecular structures,[6] and the peeling of biopolymers off of flat substrates[7] have all been studied at the single-molecule level using force spectroscopy. The use of mechanical force as an external control parameter, as demonstrated in these experiments, has made it possible to envision single molecules as a component of a microanalytical platform[8] in which high-resolution force spectroscopy can detect structural changes down to monomer resolution.

Optical tweezers and atomic force microscopy (AFM) are the most widely used techniques for the practical implementation of force spectroscopy experiments.[9] They provide both subnanonewton sensitivity in measurements of applied forces and subnanometer sensitivity in molecular extensions. The drawback of these techniques is that they require advanced (and, in the case of AFM, costly) instrumentation and achieve their high level of control usually in a serial, one-molecule-at-a-time manner. Instead, the application of force spectroscopy in routine microanalytical devices should be easy to implement in a parallel format, with no expensive consumables. Magnetic tweezers hold promise for being such a technique for the broad application of force spectroscopy in bioanalysis.[10] In magnetic tweezers, the forces are applied to molecules via superparamagnetic spherical probes using an external magnetic field. These probes, or magnetic beads, can be synthesized in bulk solutions, and some are already available commercially. With such probes, one can cover several orders of magnitude in force (from femtonewtons to tens of piconewtons), but resolution in probe displacement commensurate with molecular sizes (subnanometer) is also required, especially for shorter biopolymers.

This level of sensitivity to the movement of the probe can be achieved with an analysis of interference fringes in optical images

---

*Corresponding authors. E-mail: fridon.shubitidze@dartmouth.edu, dvezenov@lehigh.edu.

(1) Neuman, K. C.; Lionnet, T.; Allemand, J. F. *Annu. Rev. Mater. Res.* **2007**, *37*, 33.

(2) Stroh, C.; Wang, H.; Bash, R.; Ashcroft, B.; Nelson, J.; Gruber, H.; Lohr, D.; Lindsay, S. M.; Hinterdorfer, P. *Proc. Natl. Acad. Sci. U.S.A.* **2004**, *101*, 12503.

(3) Rief, M.; Gautel, M.; Oesterhelt, F.; Fernandez, J. M.; Gaub, H. E. *Science* **1997**, *276*, 1109.

(4) Ros, R.; Eckel, R.; Bartels, F.; Sischka, A.; Baumgarth, B.; Wilking, S. D.; Puhler, A.; Sewald, N.; Becker, A.; Anselmetti, D. *J. Biotechnol.* **2004**, *112*, 5.

(5) Marszalek, P. E.; Li, H. B.; Fernandez, J. M. *Nat. Biotechnol.* **2001**, *19*, 258.

(6) Embrechts, A.; Schonherr, H.; Vancso, G. J. *J. Phys. Chem. B* **2008**, *112*, 7359.

(7) Manohar, S.; Mantz, A. R.; Bancroft, K. E.; Hui, C. Y.; Jagota, A.; Vezenov, D. V. *Nano Lett.* **2008**, *8*, 4365.

(8) Albrecht, C.; Blank, K.; Lalic-Multhaler, M.; Hirler, S.; Mai, T.; Gilbert, I.; Schiffmann, S.; Bayer, T.; Clausen-Schaumann, H.; Gaub, H. E. *Science* **2003**, *301*, 367.

(9) Neuman, K. C.; Nagy, A. *Nat. Met.* **2008**, *5*, 491.

(10) Assi, F.; Jenks, R.; Yang, J.; Love, C.; Prentiss, M. *J. Appl. Phys.* **2002**, *92*, 5584.

**DOI:** 10.1021/la1015252

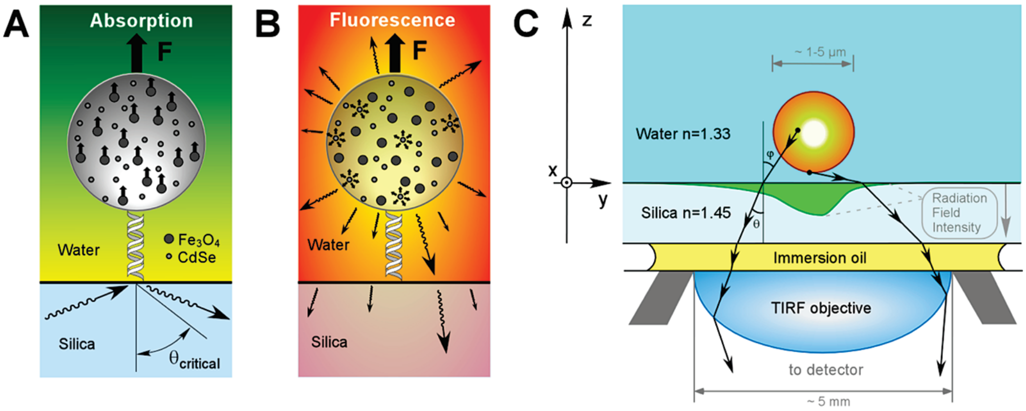

**Figure 1.** (A) Absorption of evanescent EM radiation by a fluorescent magnetic bead in water. The evanescent EM field is created by a laser beam undergoing TIR at the silica–water interface. Polystyrene beads are pulled by a magnetic field with a total force **F** resulting from the interactions (small arrows) between magnetic moments induced in individual magnetite nanoparticles and the magnetic field gradient. (B) Detectable response from the bead fluorescent component—QDs that emit in all directions (arrows)—resulting from photons that are transmitted through silica. (C) Geometry of the objective–silica–water–bead setting.

of microscopic beads[1,11] or, alternatively, by observing the optical response of the probes placed in the evanescent field near the interface where biomolecules are anchored. Singh-Zocchi et al. achieved nanometer resolution in distance from the surface for the DNA-tethered beads using an analysis of the scattering of the optical near field by dielectric microspheres.[12] Evanescent wave scattering or luminescence from colloids has become an established tool for mapping particle-surface potential energy profiles.[13,14] Therefore, photometry applied to images of magnetic microspheres excited by the optical evanescent field can potentially be used for highly sensitive measurements of molecular extensions in magnetic tweezers (Figure 1A,B).[15] To understand the fundamentals of the optical response of magnetic fluorescent microspheres, we carried out numerical simulations of electromagnetic (EM) interactions of these probes with the optical near field. We developed a body-of-revolution formulation of the method of auxiliary sources (BOR-MAS) and used it to study the absorbance, scattering, and fluorescence in a typical force spectroscopy experiment. The numerical results presented here could serve as a guide for the design and analysis of magnetic-tweezer-based force spectroscopy experiments and establish the requirements for the fabrication of the force probes.

## Approach

The evanescent EM field can be readily created in the vicinity of the solid–water interface in an optical microscope using either a prism or an objective-based total internal reflection (TIR) setup (Figure 1). The penetration depth, or characteristic decay length, of the evanescent EM field will depend on the refractive indices of the solid support and buffer solution and the laser beam wavelength and its angle of incidence.[16] In general, the penetration depth is in the range of 50–200 nm for visible light. One can use the measurement of the amplitude of the electric field at a given location in water as a means to map the distance of this location from the TIR interface. A probe that is capable of interaction with an EM field (e.g., a fluorescent dye molecule or a nanoscopic scatterer) will effectively report its position with respect to the interface when it produces a measurable photonic response (such as fluorescence). The description of the measurement of molecular extension by bead tracking requires a rigorous numerical solution of vector electromagnetic field equations because the critical dimensions (distance between the bead and solid support as well as, possibly, the size of the bead itself) are on the subwavelength scale.

For micrometer-sized probes, the waist of the incident collimated laser beam is much greater than the bead diameter; therefore, the incident electromagnetic wave can be approximated as a plane wave. In addition, the numerical aperture of a typical TIR objective is 1.45 and is the same as the refractive index of quartz or fused silica (a frequently used material with low autofluorescence, $n_D = 1.45$) substrates, which guarantees that any angles of incidence $\theta$ between critical and glancing angles (66.5 and 90°) are achievable in these substrates (Figure 1C). Notice that the use of common glass coverslips ($n_D = 1.52$) as substrates will limit the available range of angles of incidence but will not significantly affect the outcome of the simulations within that range. The choice of the angle of incidence is important in considerations of the dynamic range and sensitivity. Small angles (close to the critical angle) have a small field gradient, and large angles (close to 90°) have too short a penetration depth. In this article, we use the index of silica in order to cover the widest possible choice of conditions for incident light. Angles of 70, 75, 80, and 85° are used in calculations to investigate the dependence of the decay length on the angle of incidence.

The practical implementation of magnetic tweezers for the detection of molecular extension using TIRFM (total internal reflection fluorescence microscopy) relies on the use of probes that are several micrometers in diameter and contain a significant amount of magnetite (volumetric fraction $>20\%$) in order to approach a high force regime ($> 10$ pN) in pulling experiments.[1] A potential for long-term exposure to laser radiation favors the use of luminescent components, such as semiconducting nanocrystals, that are more resistant to photobleaching than typical fluorescent organic dyes.[17] The schematic diagram for such a bead-tracking setup is shown in Figure 1. Part of the energy in the incident wave is absorbed by the conductive bead components (magnetite and quantum dots), and the rest is either scattered

---

(11) *Handbook of Molecular Force Spectroscopy*; Noy, A., Ed.; Springer: New York, 2008.

(12) Singh-Zocchi, M.; Dixit, S.; Ivanov, V.; Zocchi, G. *Proc. Natl. Acad. Sci. U.S.A.* **2003**, *100*, 7605.

(13) Wu, H. J.; Shah, S.; Beckham, R.; Meissner, K. E.; Bevan, M. A. *Langmuir* **2008**, *24*, 13790.

(14) Everett, W. N.; Beckham, R. E.; Meissner, K.; Bevan, M. A. *Langmuir* **2007**, *23*, 8950.

(15) Liu, R. C.; Garcia-Manyes, S.; Sarkar, A.; Badilla, C. L.; Fernandez, J. M. *Biophys. J.* **2009**, *96*, 3810.

(16) Wazawa, T.; Ueda, M. *Microsc. Tech.* **2005**, *95*, 77.

(17) Sapsford, K. E.; Pons, T.; Medintz, I. L.; Mattoussi, H. *Sensors* **2006**, *6*, 925.

back into the TIRF objective or forward scattered away from the detector. This article focuses primarily on the fluorescence detection scheme because it is straightforward to implement with commercial TIRF microscopes and has an extremely favorable signal-to-noise ratio because of efficient filtering of the background radiation.[16]

The power absorbed by magnetite is dissipated, and the optical power deposited in the semiconducting quantum dots (or fluorescent organic dyes) is re-emitted at a longer wavelength. Thus, two different physical processes take place: (a) absorption and scattering and (b) fluorescence. To understand the underlying physics of each of these processes, using the BOR-MAS model we separate the interaction of light with the bead into two steps: (i) an absorption and scattering stage and (ii) a fluorescence stage. The strength of the fluorescence signal depends on the composition of the bead, the material properties of each of the components, the incident power, and the out-of-plane ($z$) position of the bead. In the fluorescence stage, the EM waves emitted by quantum dots (QDs) escape the bead, undergoing absorption by magnetite on their way and are collected by the microscope objective to yield the final image. The premise behind this setup is that one can use the total intensity of this fluorescent image to determine the $z$ position of the bead and, therefore, the end-to-end extension of the biomolecule under a given force. The goal of the present work is to develop the formalism for the analysis of this EM problem and quantify the interaction of the micrometer-sized beads with the optical near field as a function of the bead size, location in the field, and composition.

**Dielectric Constants of the Microscopic Probes.** Synthesized beads consist of randomly oriented, complex-shaped nanoparticles of magnetite ($Fe_3O_4$) and CdSe QDs, resting in a base polystyrene dielectric. The rigorous solution of an EM wave-scattering problem would account for the shape, position and orientation of these particles, a process that requires enormous amounts of computational power and time. In fact, little insight would be gained from the exact solution of the EM problem at a high level of detail for any particular bead realization. Rather, of interest to us is the general behavior of the composite bead that depends only on a limited number of macroscopic properties (such as the volumetric fraction of nanoscopic components and their EM properties). There have been several attempts to account analytically for the random shape and position of small inclusions in a medium and derive the effective properties of the composite media,[18] with variable rates of success. The comparison and description of these effective medium models is a separate active research topic[19,20] and is beyond the scope of this article. Because empirically most of these models, none being exact, result in similar predictions of effective medium properties, it is sufficient to perform the entire analysis based on a single model.

For the purposes of this article, we assume that for the majority of real-life scenarios the embedded conductive particles can be considered to be spherical and spread randomly in a linear isotropic medium. In this case, the Maxwell–Garnett[20] model gives the following prediction of the effective dielectric permittivity $\varepsilon_{\text{eff}}$ of the bead as a whole

$$\varepsilon_{\text{eff}} = \varepsilon_{\text{b}} + \frac{3\varepsilon_{\text{b}} \sum_{i=1}^{n} f_i \dfrac{(\varepsilon_i - \varepsilon_{\text{b}})}{(\varepsilon_i + 2\varepsilon_{\text{b}})}}{1 - \sum_{i=1}^{n} f_i \dfrac{(\varepsilon_i - \varepsilon_{\text{b}})}{(\varepsilon_i + 2\varepsilon_{\text{b}})}} \qquad (1)$$

where $f_i$ is the volumetric fraction of the $i$th spherical inclusion having a dielectric constant $\varepsilon_i$, in a base material of the dielectric constant $\varepsilon_{\text{b}}$. (See sections 1 and 2 of Supporting Information for a discussion of the applicability of the Maxwell–Garnett model and a calculation of the refractive index.)

The power per unit volume absorbed by the inclusions can be estimated from the calculated local field $\mathbf{E}_{\text{L}}$ that excites the $i$th inclusion (with volume $V_i$, concentration $n_i$, and conductivity $\sigma_i$) using the following expression ($V$ is the total volume):

$$\mathbf{P}_i = \frac{V_i n_i}{V} \mathbf{j}_i \mathbf{E}_{\text{L}} = f_i(\sigma_i \mathbf{E}_{\text{L}})\mathbf{E}_{\text{L}} = f_i \sigma_i {\mathbf{E}_{\text{L}}}^2 \qquad (2)$$

Equation 2, derived under the same assumptions as for the Maxwell–Garnett formula (section 3 of Supporting Information), can be used to determine the fraction of power absorbed by each of the components in the mixture. The fraction of power absorbed by QDs is emitted back as a fluorescence signal and is weighted by both their volumetric fraction and conductivity. Although we use CdSe QDs as specific luminophores in our system, the results are directly applicable to other emitters when the optical power is rescaled according to their volume fraction and conductivity.

**Near-Field Optics.** We used the method of auxiliary sources (MAS) to determine the near- and far-field responses of the lossy dielectric bead in the evanescent electromagnetic field. (A copy of the program can be obtained by contacting the authors.) The MAS, which belongs to the generalized multipole technique family,[21] is a numerical technique for a rigorous solution of Maxwell's equations. The method is easy to implement and has been successfully applied to electromagnetic scattering and radiation problems.[22–24] The backbone of the method is the idea of representing the field in the domains of interest by expanding it into a finite series of fields produced by elementary auxiliary sources located inside and outside the boundaries of the physical object. These auxiliary sources are usually placed on surfaces that are conformal to the actual surface of the object and have a uniform distribution. Auxiliary sources outside of the object are responsible for the representation of the inner field, and sources inside the object boundary produce the field outside that boundary, thus singularities are never encountered. Because the wave function of each of the auxiliary sources represents a solution of the wave equation, the only requirement imposed on these sources is to satisfy the boundary conditions, namely, the continuity of tangential components of electric and magnetic fields on both sides of the physical surfaces.

Shubitidze et al. described an effective optimization of the MAS for quasi-magnetostatic problems with cylindrical symmetry.[23] By expanding the fields into a Fourier series in the azimuthal direction (angle $\varphi$, Figure 2), one can significantly reduce the dimensionality of the problem. Instead of a 3D problem with unknown auxiliary sources distributed across surfaces, we now have a 2.5D problem, with unknowns distributed along a 2D line. The added cost, expressed effectively as an extra 0.5 dimension, is from the need to perform a separate calculation for each of the spatial Fourier components in the azimuthal direction in the incident field. In this article, we extend the body of revolution formulation of the MAS for a general case of EM fields of arbitrary frequency.

---

(18) Sihvola, A. H.; Kong, J. A. *IEEE Trans. Geosci. Remote Sens.* **1988**, *26*, 420.

(19) Zhou, P. H.; Deng, L. J.; Wu, B. I.; Kong, J. A. *Prog. Electromagn. Res.* **2008**, *85*, 69.

(20) Sihvola, A. *Subsurf. Sens. Technol. Appl.* **2000**, *1*, 393.

(21) Wriedt, T. *Generalized Multipole Techniques for Electromagnetic and Light Scattering*; Elsevier: Amsterdam, 1999.

(22) Shubitidze, F.; Anastassiu, H. T.; Kaklamani, D. I. *IEEE Trans. Antennas. Propag.* **2004**, *52*, 302.

(23) Shubitidze, F.; O'Neill, K.; Haider, S. A.; Sun, K.; Paulsen, K. D. *IEEE Trans. Geosci. Remote Sens.* **2002**, *40*, 928.

(24) Shubitidze, F.; O'Neill, K.; Sun, K.; Shamatava, I.; Paulsen, K. D. *Appl. Comput. Electromag. Soc. J.* **2004**, *19*, 112.

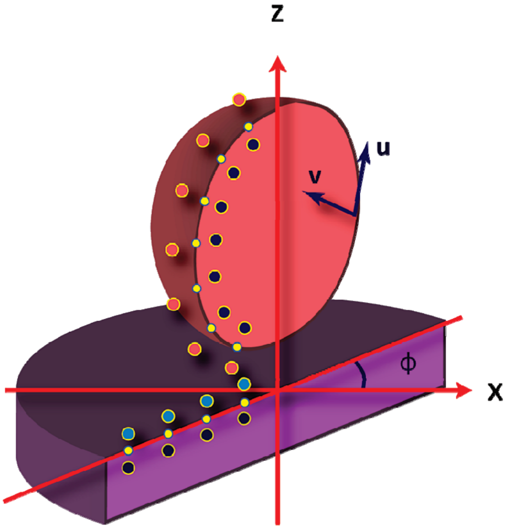

**Figure 2.** Cross-section of the body of revolution objects (the bead and semi-infinite half-space) with their boundary collocation points (small yellow dots), internal (black) and external (blue and red) auxiliary sources and surface tangents (**u** and **v**) used for the boundary field projection and auxiliary source alignment.

According to the conventional MAS procedures, we first allocate a set of uniformly distributed collocation points on the surfaces of interest and define two conformal surfaces holding auxiliary sources—one inside and one outside the object (Figure 2). Every point on the surface hosts two orthogonal auxiliary sources whose wave functions already satisfy Maxwell's equations (i.e., electric dipoles and magnetic dipoles). Auxiliary sources that describe EM fields in a certain region are located outside of that region, on a surface conformal to its boundary. Typically, the positions of auxiliary sources are obtained by sliding up and down along the surface normals at the boundary collocation points. Such placement helps to avoid singularities in the solution because the fields are always evaluated at a finite distance from the source origin.

Let the index $n = 1, 2,..., N$ identify a horizontal belt of collocation points obtained by rotating the individual surface collocation points shown as yellow dots in the Figure 2 around the $z$ axis. Let $\mathbf{u}_n(\varphi)$ and $\mathbf{v}_n(\varphi)$ be the vectors, tangent to the object surface, used for both the auxiliary source alignment and the EM field projection. The fields $\mathbf{F}_{\mathrm{id}}$ inside the object at point $\mathbf{r}$ are then represented as follows

$$\mathbf{F}_{\mathrm{id}}(\mathbf{r}) = \mathbf{F}_{\mathrm{id}}^{\mathrm{src}}(\mathbf{r}) + \sum_{n \in N_{\mathrm{id}}} \oint_0^{2\pi} \mathrm{d}\varphi \sum_{\boldsymbol{\tau}=\{\mathbf{u},\mathbf{v}\}} [P_{\boldsymbol{\tau},n}(\varphi)\, \mathbf{G}_{\mathrm{F}}(\mathbf{r}, \mathbf{r}_n | \boldsymbol{\tau}_n(\varphi))] \tag{3}$$

where $\mathbf{F}_{\mathrm{id}}^{\mathrm{src}}(\mathbf{r})$ represents fields (electric or magnetic) generated by the independent sources in the domain [id = (silica, water, bead)], $N_{\mathrm{id}}$ is the number of auxiliary sources that produce EM fields in the domain, $P_{\tau,n}(\varphi)$ is the auxiliary source amplitude density within the belt, and $\mathbf{G}_{\mathrm{F}}(\mathbf{r}, \mathbf{r}_0|\boldsymbol{\tau})$ represents the electric ($\mathbf{F} = \mathbf{E}$) and magnetic ($\mathbf{F} = \mathbf{H}$) fields created at point $\mathbf{r}$ by a unit elementary dipole located at $\mathbf{r}_0$ and oriented along $\boldsymbol{\tau}$ (= $\mathbf{u}$ or $\mathbf{v}$)

$$\mathbf{G}_{\mathrm{E}}(\mathbf{r}, \mathbf{r}_0|\boldsymbol{\tau}) = \left[\frac{3\mathbf{R}(\mathbf{R}\boldsymbol{\tau}) - \boldsymbol{\tau}\mathbf{R}^2}{R^5}(1 - jkR) - \frac{k^2\mathbf{R} \times (\mathbf{R} \times \boldsymbol{\tau})}{R^3}\right] \frac{\mathrm{e}^{jkR}}{4\pi\varepsilon\varepsilon_0} \tag{4}$$

$$\mathbf{G}_{\mathrm{H}}(\mathbf{r}, \mathbf{r}_0|\boldsymbol{\tau}) = \left[\frac{1}{R^2} - \frac{jk}{R}\right](\mathbf{R} \times \boldsymbol{\tau}) \frac{jk_0 \mathrm{e}^{jkR}}{4\pi R(\mu_0\varepsilon_0)^{1/2}} \tag{5}$$

where $\mathbf{R} = \mathbf{r} - \mathbf{r}_0$ is the relative distance of the target from the source, $k = k_0(\varepsilon)^{1/2}(\mu)^{1/2}$ is the wavenumber, with $k_0$ being that in free space, and $\{\varepsilon, \mu\}$ is the relative dielectric permittivity and magnetic permeability of the domain medium.

According to EM field boundary conditions, the following vector equations should be satisfied at every point of real object surfaces

$$\mathbf{n} \times \mathbf{E}_{in} = \mathbf{n} \times \mathbf{E}_{out} \tag{6a}$$

$$\mathbf{n} \times \mathbf{H}_{in} = \mathbf{n} \times \mathbf{H}_{out} \tag{6b}$$

where $\mathbf{n} = \mathbf{v} \times \mathbf{u}$ is the surface normal and the corresponding field vectors are evaluated separately for the two domains bounded by the surface. Therefore, to solve the scattering problem and evaluate fields over the entire space, one has to solve a single system of linear equations for unknown amplitudes of auxiliary sources, arising from boundary conditions (eq 6).

For the body of revolution (BOR) problems, we can account for the $\varphi$ dependence of incident fields and amplitudes of auxiliary sources by expanding the fields into a Fourier series in the azimuthal direction

$$\mathbf{F}_{id}(\mathbf{r}) = (\sum_{L=0}^{\infty}(\mathbf{F}_{id,L}^{C}(\rho, z)\, cos(L\varphi) + \mathbf{F}_{id,L}^{S}(\rho, z)\, sin(L\varphi)) \tag{7a}$$

$$P_{\tau,n}(\varphi) = \sum_{L=0}^{\infty}(P_{\tau,n,L}^{C}\, cos(L\varphi) + P_{\tau,n,L}^{S}\, sin(L\varphi)) \tag{7b}$$

where $\mathbf{r} = \mathbf{r}(\rho, z, \varphi)$ is in the cylindrical system of coordinates, $\mathbf{F}_{id,L}^{\{C,S\}}$ represents the Fourier coefficients for incident fields in the domain $id$, $P_{\boldsymbol{\tau},n,L}^{\{C,S\}}$ represents Fourier coefficients for amplitudes of the auxiliary sources, and $L$ is the spatial mode in the azimuthal direction. Because the spatial distribution of the currents induced in the system depends on the behavior of the driving external EM field, the substitution of Fourier expansions (eq 7) into boundary conditions (eq 6), evaluated at a set of uniformly distributed collocation points along the object boundaries, will yield $2L+1$ independent systems of $4 \times N$ linear equations for the unknown Fourier amplitudes $P_{\boldsymbol{\tau},n,L}^{\{C,S\}}$ of auxiliary sources (one system of equations for each cos($L\varphi$) and sin($L\varphi$) mode along with that for the zeroth mode). Once these amplitudes are found, any other EM parameter of interest (power flow, near and far fields, distribution of excited volumetric currents inside lossy objects, etc.) can be derived through the superposition of fields created by real and auxiliary sources. This scheme also provides an easy way to monitor the accuracy of the numerical solution by inspecting the mismatch of boundary conditions resulting from inner and outer auxiliary sources.

The benefit of the MAS formalism is that, besides the original source of radiation (the incident EM wave), it allows for the consideration of any number of additional EM field sources both inside and outside the object of interest, thus making modeling of the fluorescence straightforward. Because the wave fields of each of the auxiliary sources satisfy the wave equation exactly, the only source of error arises from the imperfect satisfaction of the boundary conditions as a result of the discretization of the distribution of auxiliary sources. The major obstacle to the efficiency of the method arises from the large number of auxiliary sources needed to precisely identify the fields inside and outside of the microsphere and the unknown deviations of auxiliary surfaces from real geometry. Using the BOR approximation reduces the number of unknown auxiliary source amplitudes from $4N \times M$ to $4N$ (where $M$ is the average number of collocation points required to cover object surfaces in the azimuthal direction for each of the $N$ belts), significantly decreasing the size of the system of linear

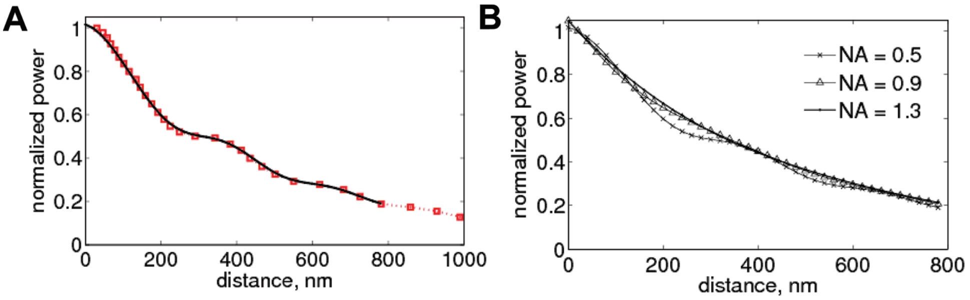

**Figure 3.** Intensity of 658 nm light forward scattered from a 1.35-$\mu$m-diameter polystyrene bead in water ($n_{\text{water}} = 1.333$) versus the distance from the glass substrate ($n_{\text{glass}} = 1.515$). TIR wave penetration depth $\delta_p = 500$ nm ($\theta = 62.0°$). (A) The solid line indicates the results of our simulations, and the dotted line with square markers (red in online version) represents the experimental data.[25] (B) Simulations of optical power observed by objectives with varying NA. The power is normalized to the maximum intensity observed when the bead is effectively in contact with the surface.

equations. This reduction, however, comes at the expense of the requirement to solve the EM problem separately for each of the spatial Fourier components in the azimuthal direction ($L = 0$, 1, ..., $L_{\max}$, where $L_{\max}$ is the highest mode number whose value depends on the specific character of the incident field).

The major advantage of BOR with respect to the full 3D model becomes obvious when the full complexity of the problem, mimicking a potential experimental application, is considered; namely, to account for the presence of the nearby interfaces (e.g., multilayered substrates) and other material layers (e.g., core−shell structure of the probes), it is necessary to place a large number of auxiliary EM field sources across these interfaces. The BOR approximation, by reducing the problem dimensionality, makes it possible to use a reasonable number of auxiliary sources and provides an accurate solution within reasonable time limits (approximately 3−5 h per case on a present-day desktop PC).

## Results and Discussion

**Calculation of the Absorbed, Scattered, and Fluorescently Emitted Power.** The MAS approach allows the efficient computation of energy transfer through surfaces of the bead or silica by numerically evaluating the integral of the Poynting vector flux across these surfaces

$$\mathscr{P} = \oint_{\text{surface}} \frac{1}{2} Re\{\mathbf{E} \times \mathbf{H}^*\}\, d\mathbf{S} \tag{8}$$

where **E** is the electric field and **H*** is a complex conjugate of the magnetic field phasor. On one hand, during the absorption stage, because there are no EM field sources inside the bead, the integration across the bead surface will yield the total power absorbed inside the bead. On the other hand, during the fluorescence stage, this integral yields the total power emitted by quantum dots.

Of more interest, however, is the part of the observable radiation (i.e., either the incident power scattered by the bead or the part of the power re-emitted by the fluorophores that reaches the microscope objective after passing through the silica substrate). For incident rays leaving the objective, the numerical aperture is (Figure 1) NA $= n_{\text{solid}} \sin(\theta_{\max}) = n_{\text{water}} \sin(\varphi_{\max})$, where $\theta_{\max}$ and $\varphi_{\max}$ are beam propagation angles in the solid substrate and water, respectively. If NA $= n_{\text{silica}} = 1.45$, then essentially any incident angle in silica, (i.e., any value of $\theta$ from 0 to 90°) is achievable. According to the reciprocity theorem and taking into account that the entrance pupil of the objective is much greater than the area of interest (millimeter vs micrometer scale, respectively), it is also true that any ray entering the silica through the water−silica interface ends up in the objective. Therefore, to find the total energy transformed into the image of the bead, we integrate the Poynting vector flux (eq 8) across the water−silica interface within the finite area directly underneath the bead. The re-radiated field decays quickly with distance, and the area of $10\lambda$ in radius is usually sufficient to capture the total flux through silica to high accuracy. In general, however, for objectives having a smaller NA, one would have to limit the area of integration to be consistent with the numerical aperture of the microscope objective.

Two separate MAS simulations are required to account for the underlying two-stage physical processes of the described experiments. In the first stage, the bead, having effective medium properties, is excited by the incident evanescent electromagnetic field, and the volumetric distribution of currents inside the bead is calculated. In the second stage, these volumetric currents are rescaled according to eq 2 in order to account for power deposited in quantum dots only and used further as excitation to simulate bead fluorescence at a higher wavelength. (See section 4 of the Supporting Information for a discussion of the issue of dealing with the phase distribution of bead volumetric currents.)

To verify the accuracy of our numerical simulations, we compared the forward-scattering simulations on pure polystyrene beads to published experimental data.[25] In these experiments, the scattering fields were observed far away above the bead, in the positive $z$ direction (Figure 1), after passing through a linear polarizer using an objective with an NA of 0.5.[26] To simulate the truncation of the scattered waves by the objective, we calculated far-field distributions in polar coordinates and integrated optical power over angles captured by the 0.5 NA objective. We found excellent agreement with the existing data (Figure 3A). Our simulations also show that for high-NA objectives the power−distance relation approaches exponential behavior. This change in behavior is illustrated in Figure 3B, where the far-field pattern of the scattering field is integrated within the spherical angles corresponding to objectives with NA = 0.5, 0.9, and 1.3. The accuracy of our MAS simulations was further confirmed by excellent matching of boundary conditions on bead and silica surfaces for both absorption and fluorescence stages (section 5 of Supporting Information).

**Field and Power Distributions.** Figure 4A,C shows 2D electric field distributions in the planes containing the center of the bead for TE polarization. (See section 6 of Supporting

---

(25) Hertlein, C.; Riefler, N.; Eremina, E.; Wriedt, T.; Eremin, Y.; Helden, L.; Bechinger, C. *Langmuir* **2008**, *24*, 1.

(26) Riefler, N.; Eremina, E.; Hertlein, C.; Helden, L.; Eremin, Y.; Wriedt, T.; Bechinger, C. *J. Quant. Spectrosc. Radiat. Transfer* **2007**, *106*, 464.

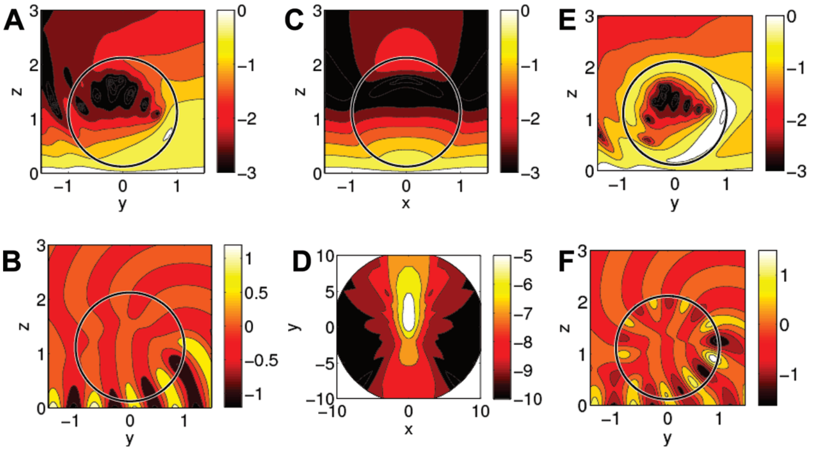

**Figure 4.** Electric field, phase, and power distribution for a 1-$\mu$m-diameter bead containing 20% $Fe_3O_4$ and 5% (A−D) or 40% (E, F) CdSe QDs positioned 60 nm away from the silica−water interface, illuminated by a TE-polarized 532 nm beam incident at 75°. All coordinates are in units of bead radius, the color scale in A, C, D, and E is logarithmic, and $|E_{inc}| = 1$ for the incident field. (A) Absolute $E$ field distribution in the $yz$ plane. (B) $E_x$ phase distribution in the $yz$ plane. (C) Absolute field distribution in the $xz$ plane. (D) Distribution of power scattered through silica in the $xy$ plane. (E) Absolute $E$ field distribution in the $yz$ plane on a log scale. (F) $E_x$ phase distribution in the $yz$ plane.

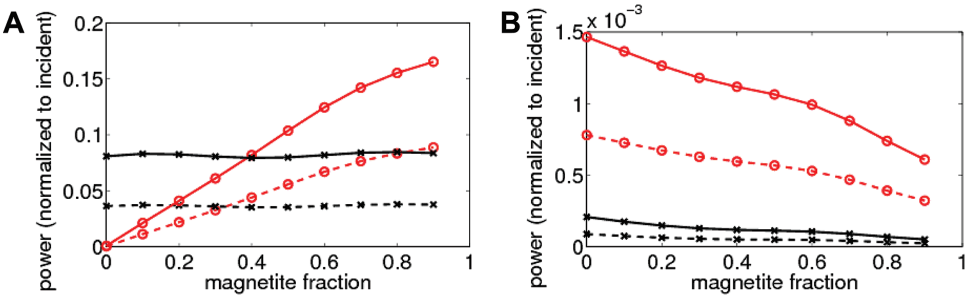

**Figure 5.** (A) Power deposited in the bead (o) and scattered through the silica substrate (×) during the absorption stage (TE polarization, $\lambda$ = 532 nm). (B) Total fluorescence power leaving the bead (o) and detectable fluorescence power (×) ($\lambda$ = 597 nm). All power is plotted as a function of bead magnetite concentration (QD volume fraction is constant at 5%, angle of incidence $\theta$ is 75°, bead diameter is 1.0 $\mu$m). Solid and dotted lines correspond to beads positioned 30 and 90 nm away from silica. The powers are normalized by the total power available from the incident beam in the silica substrate (for the circular cross-sectional area with a radius equal to the bead radius).

Information for TM polarization.) Each distribution has the expected evanescent character with field amplitude around the sphere decaying away from the silica−water interface, although the presence of the bead noticeably perturbs the original field distribution, which is laterally uniform.

There is a significant increase in the optical field intensity in the bead itself as a result of waveguiding: because the refractive index of the bead is higher than that of water, the traveling wave can be formed in both $y$ and $z$ directions inside the bead, and as a result, the field intensity wraps around polymer−water interface along the bead circumference. Figure 4A,C indicates that most of the incident power will be deposited in the quantum dots closest to the silica−water interface because electric fields are highest in the vicinity of the interface. The area with the least power absorption is in the middle of the bead. Qualitatively, the fields are similar for both TE and TM excitation polarizations, although the detectable fluorescence power in TE is ∼50% greater than that in TM polarization (cf. Figures 4B and S5B in Supporting Information). Figure 4D, showing the power flux across the water−silica interface, indicates a significant power drop with distance from the bead along the silica surface (a 10-fold decrease occurs about 2 $\mu$m away from the bead). This observation supports the assumption that, for a high NA objective, to find the total power transmitted by the light that forms the image of the bead it is sufficient to integrate the Poynting vector flux over the appropriate finite area on the silica surface.

**Power as a Function of Bead Composition.** The amount of power absorbed in a microsphere and emitted back is nonlinear with changes in the bead composition and distance from the surface, as shown in Figure 5A,B for TE-polarized excitation. (See section 6 of Supporting Information for TM polarization.) Only at small loads of magnetite and QDs does the power absorbed change approximately linearly with the amount of the two nanoscopic components. Because practical considerations call for high magnetite content (to achieve high force sensitivity) but require a relatively modest amount of fluorescent material for adequate detection, the behavior of the beads containing 10−40% (volume) magnetite and 5% (volume) QDs is considered to be representative of the probes designed for magnetic tweezers. For a bead with 5% luminescent inclusions, we observed that whereas the absorbed power indeed increased approximately linearly with the amount of magnetite the scattering intensity remained approximately constant (Figure 5A). In spite of more power being absorbed by the bead when the concentration of magnetite increased, the amount of fluorescence has steadily decreased (Figure 5B), consistent with the expectation that most of the increase in absorption is due to absorption by magnetite only. The increased amount of magnetite also resulted in the screening of fluorescence from the quantum dots. However, the overall reduction was moderate: an increase in the amount of magnetite from 0 to 50% resulted in a reduction in fluorescence by only 25% from its initial value in the nonscreened case. The data

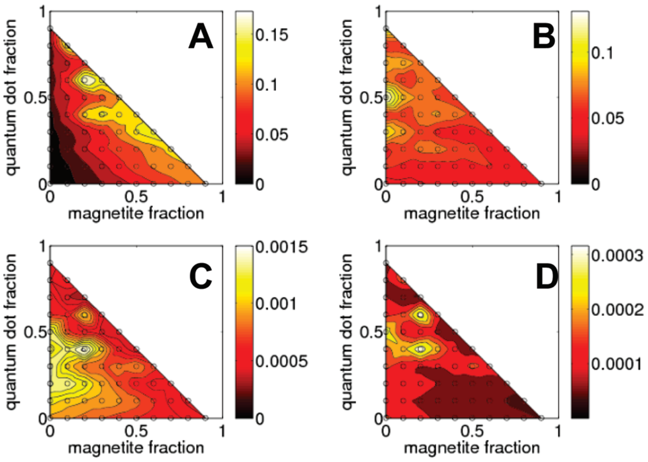

**Figure 6.** Power deposited in spheres (A) and scattered through silica (B) in the absorption stage; power emitted from the sphere (C) and transmitted through silica (D) in the fluorescence stage. All power is plotted as a function of magnetite and QD volume fractions. (TE polarization, $\theta = 75°$, bead diameter is 1.0 $\mu$m, distance from silica is 60 nm, incident $\lambda = 532$ nm, fluorescence $\lambda = 597$ nm).

in Figure 5 indicates that these general trends are true for various bead–silica distances and incident TIR wave polarizations. The further the bead is from the silica surface, the less power that is absorbed, scattered, and re-emitted.

As seen in Figure 5, for a typical probe with a 0.1–0.3 volume fraction of magnetite, less than 7% of the total incident power is absorbed and 3% of the absorbed power is re-emitted as fluorescence, with 10–15% of the total fluorescence eventually reaching the detector. Because then the total efficiency of conversion of the incident optical power to fluorescence for a micrometer-sized sphere is around $10^{-4}$, it is clear that the signal-to-noise ratio in bead tracking can be significantly improved by reducing undesired absorbance (by magnetite) or by improvements in fluorescence properties. A significant input of power dissipated as heat can also potentially lead to undesirable local heating of the probe. Interestingly, the scattering intensity changes little with magnetite composition and can direct a significant amount ($\sim$8%) of the incident power to the detector.

We have also surveyed the changes in the photonic response of the probes over the entire range of composition by varying the volume fraction between 0 and 1 for both magnetic and luminescent components. The results of such a global calculation for a 1.0-$\mu$m-diameter bead shown in Figure 6 demonstrate that, while the overall absorption and fluorescence scale as expected with the amount of optically active materials, the observable scattering and fluorescence experience changes relatively moderately (within a factor of 2) for a wide range of compositions.

As illustrated in Figure 6B, the amount of power at the original wavelength of incident light scattered by the bead and traveling back to the objective is significant. The power emitted during the fluorescence stage, although several orders of magnitude lower than the elastically scattered power, can be effectively filtered from the illuminating and scattered power and readily detected using commercial TIRF microscopes.

A substantial increase in fluorescence is apparent in Figure 6C, D for a bead containing approximately 20% magnetite and 40% quantum dots compared to most other compositions. The field distribution for this case is shown in Figure 4E: although qualitatively it is similar to distributions shown in Figure 4A (i.e., the highest field is observed inside the part of the bead that is closest to the TIR interface), a certain resonance clearly takes place—a relatively high field is present inside an entire bead near its surface. This resonance condition leads to efficient coupling of the optical power from the incident beam into waveguided modes of the bead (whispering gallery modes), which results in more power being absorbed and emitted by the bead. Although this particular bead composition having a high quantum dot content is hardly practical, such a distribution of near fields concentrated close to the surface of the bead may be useful in layered structures. The beads consisting of a magnetic core surrounded by a layer of fluorescent material would effectively guide and store the incident waves solely in the fluorescent components, eliminating the unnecessary energy losses in the magnetic material.

**Intensity of the Probe Image.** Because the brightness of the fluorescing microsphere is used as a quantitative measure of its distance from the silica–water interface (i.e., molecular extension), an understanding of how various experimental factors influence this signal-distance dependence is important for bead-tracking experiments. An exponential drop in a far-field image intensity, consistent with a standard two-media TIR model, is expected for a pointlike probe; however, with finite-sized probes, because of the presence of multiple interfaces, the exact nature of changes in the decay length for both scattering and fluorescence is hard to predict without numerical solutions. As Figure 4 demonstrates, the electric field distribution in and around the bead is perturbed so significantly from the exponentially decaying field distribution in the case of a planar interface that estimates based on a simple TIR model should not be viewed as reliable *a priori.* For a given probe of a fixed composition, the size of the probe could potentially change the characteristic decay length even for the same angle of incidence.

Figure 7A shows the results of the calculation of absorbed and observed scattering power for a 1-$\mu$m-diameter bead as a function of the bead displacement (depth) from the point of contact with the surface. Both types of curves display an exponential dependence but with different decay constants: 96.7 nm for absorbance and 80.0 nm for scattering at an angle of incidence of 75°.

The characteristic penetration depth for unperturbed EM field intensity is equal to 96.5 nm. The total fluorescence output from the bead and part of the fluorescence detectable as the probe image (flux through the silica–water interface) also scales exponentially with the separation from the surface of the sample (Figure 7B). These two curves have decay constants that mimic those for absorption and scattering. The effective decay length for observed fluorescence is noticeably smaller than the penetration depth of the evanescent field. These observations confirm the intuitive notion that the total intensity of a microsphere image (in either scattering or fluorescence mode) can serve as an unambiguous measure of the position of a microsphere with respect to the silica surface. One has to avoid, however, the direct use of the penetration depth of the evanescent field, calculated using simple models, in these intensity versus distance relations without experimental verification of such calibration curves.

A higher angle of incidence will lead to a steeper attenuation of the field in the transmission medium, and we expect to see a decrease in the decay length for bead intensity versus distance from the surface as the angle of incidence increases. Calculations for a 1-$\mu$m-diameter bead confirm this dependence (Table 1); the decay length for observed fluorescence dropped from 98.2 to 59.9 nm when the angle of incidence increased from 70 to 85°. Overall, the change in the decay length was consistent with predictions of the simple analytical TIR model; however, the observed effective penetration depth was only two-thirds of the value for the unperturbed case. The overall intensity of the bead

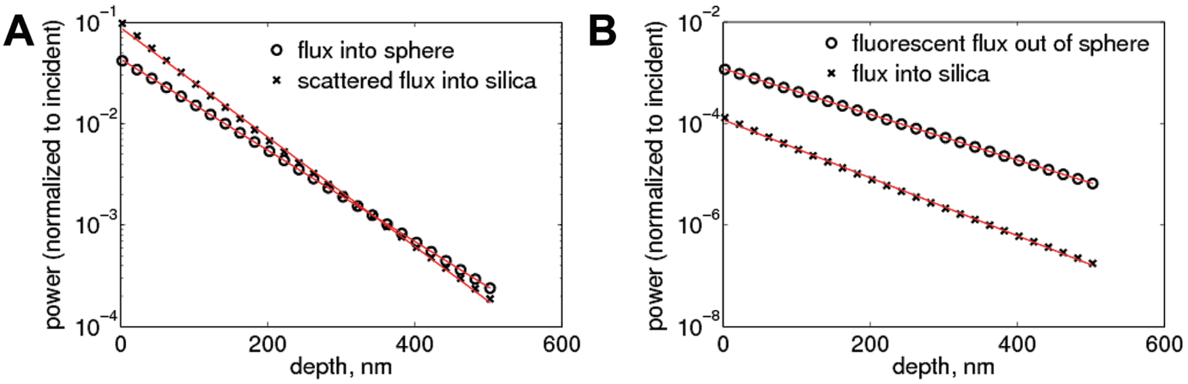

**Figure 7.** Distance calibration curves of intensity versus bead position (symbols, simulations; lines, fits to exponentials): (A) optical power deposited in the bead and scattered through silica in the absorption stage; (B) total fluorescence power leaving the bead along with detectable power passing through silica; all power is shown as a function of the bead−surface distance (20% $Fe_3O_4$ and 5% CdSe, $\theta = 75°$, bead diameter is 1.0 $\mu$m).

**Table 1. Effective Decay Lengths (nm) for Different TIR Angles of Incidence**[a]

| | | absorption stage | | fluorescence stage | |
|---|---|---|---|---|---|
| TIR angle of incidence $\theta$ (deg) | unperturbed $\delta_p$ | sphere absorption | scattering into silica | sphere fluorescence | transmission into silica |
| 70 | 143.0 | 141.0 | 104.4 | 141.5 | 98.2 |
| 75 | 96.5 | 96.7 | 80.0 | 96.4 | 75.5 |
| 80 | 81.5 | 81.3 | 66.4 | 80.9 | 63.0 |
| 85 | 75.0 | 74.9 | 62.9 | 74.8 | 59.9 |

[a] $\lambda = 532$ nm, TE polarization, bead diameter = 1 $\mu$m.

**Table 2. Effective Decay Length and Optical Power as Functions of the Bead Diameter**[a]

| diameter<br>process | 200 nm | 400 nm | 600 nm | 800 nm | 1000 nm | 1400 nm |
|---|---|---|---|---|---|---|
| Decay Length (nm) | | | | | | |
| sphere absorption | 96.0 | 96.2 | 96.1 | 96.0 | 96.7 | 96.3 |
| observed scattering | 84.2 | 84.0 | 80.8 | 78.5 | 80.0 | 76.1 |
| sphere fluorescence | 96.5 | 96.5 | 96.2 | 96.1 | 96.4 | 94.9 |
| transmitted fluorescence | 83.9 | 82.9 | 78.8 | 76.6 | 75.5 | 68.2 |
| Maximum Optical Power (Probe at $z = 2$ nm) | | | | | | |
| sphere absorption | 0.011 | 0.052 | 0.117 | 0.203 | 0.317 | 0.699 |
| observed scattering | 0.020 | 0.181 | 0.386 | 0.553 | 0.707 | 1.00 |
| sphere fluorescence ($\times 10^2$) | 0.005 | 0.078 | 0.235 | 0.499 | 0.780 | 1.45 |
| transmitted fluorescence ($\times 10^2$) | 0.003 | 0.034 | 0.068 | 0.102 | 0.103 | 0.108 |

[a] $\lambda = 532$ nm, TE polarization, $\theta = 75°$, and bead composition is 5% QDs and 20% magnetite. The fluorescence power is scaled up by a factor of 100 for ease of comparison.

also decreased dramatically because the field was confined to a narrowing volume in the vicinity of the silica surface as the angle increased. A smaller excitation volume at high angles resulted in a lower image intensity compared to that for angles of incidence that were closer to the critical angle.

At a fixed angle of incidence, the change in the size of the probes could also lead to changes in the excitation volume and the observed integrated intensity of the bead (Table 2). The total optical power absorbed and re-emitted by the beads in the size range that we studied (diameter $D = 0.2-1.4\,\mu$m) scales approximately as $D^{2.2}$. The observed total scattering or fluorescence power, however, scales approximately linearly with bead size, with the intensity of fluorescence showing a saturation for $D > 0.8\,\mu$m. The results for beads of different sizes compiled in Table 2 illustrate the effect of the probe size on the observed decay length and show that, whereas the overall intensity grows rapidly with the increase in the bead diameter, the decay length varies slowly. This approximate constancy of the decay length is important because it provides a natural way to deal with limited polydispersity in a typical sample of such beads. If the intensity of the probe images is normalized to their intensity at the point of contact, then these normalized images for all microspheres in a given sample should be representative of their position with a single decay length (within 1 to 2%) as long as the polydispersity is limited to about ±10%.

## Conclusions

The use of magnetic fluorescent force probes illuminated in the near-field regime in magnetic tweezers is a promising approach to measuring molecular dimensions. The MAS can uncover fundamentals of the photonic response at the subwavelength level of detail in these bead-tracking experiments using TIRFM. We used the cylindrical symmetry of the system to reduce the dimensionality of the problem and enable efficient, accurate calculations with minimal computational resources (desktop PC). Our studies demonstrated that for high-NA objectives the total intensity of the bead image, because of either backscattering or fluorescence transmitted into silica, showed an exponential decay with increasing distance from the surface. Decay lengths of powers absorbed and reemitted from the bead are similar to the penetration depth of evanescent waves at a given angle of incidence. However, the decay length of observable power (i.e. scattered or fluorescent radiation transmitted through the silica−water interface) is smaller (by as much as 20−30%) than the penetration depth of the excitation evanescent wave. The discrepancy between the penetration depth of the evanescent field and the effective decay length observable with the TIRFM setup, and variations in the decay length due to changes in bead size, emphasize the need to calibrate every representative probe used in the experiment if quantitative information on the bead position is required.

We believe that the new body-of-revolution formulation of the method of auxiliary sources described here (i) can be used further in exhaustive simulations of complex multilayered systems (both beads and surfaces) and (ii) can help guide efforts in the design and fabrication of optimized probes or in improvements to experimental configurations for bead tracking and single-molecule-manipulation experiments. The BOR-MAS method should be useful in the analysis of similar problems involving near field and subwavelength-sized objects, for example, in simulations of light transmission through subwavelength holes in metal films or the excitation of individual emitters in such wells.

**Acknowledgment.** This work was supported by NIH grant R21 HG004141.

**Supporting Information Available:** Limitations of the effective medium (Maxwell−Garnett) model; refractive indices of optically active component materials−magnetite ($Fe_3O_4$) and quantum dots (CdSe); separation of optical power absorbed in magnetite and quantum dots; numerical simulation of fluorescence; verification of solution accuracy through boundary conditions; and distributions of the electrical field and optical power for TM polarization of the incident beam. This material is available free of charge via the Internet at http://pubs.acs.org.